Journal of Biomedical Optics

SPIEDigitalLibrary.org/jbo

High-resolution optoacoustic mesoscopy with a 24 MHz multidetector translate-rotate scanner

Jérôme Gateau
Andrei Chekkoury
Vasilis Ntziachristos

SPIE

High-resolution optoacoustic mesoscopy with a 24 MHz multidetector translate-rotate scanner

Jérôme Gateau, Andrei Chekkoury, and Vasilis Ntziachristos
Technische Universität München and Helmholtz Zentrum München, Institute for Biological and Medical Imaging, Ingoldstädter Landstraße 1, 85764 Neuherberg, Germany

Abstract. Optoacoustic (photoacoustic) mesoscopy aims at high-resolution optical imaging of anatomical, functional, and cellular parameters at depths that go well beyond those of optical-resolution optical or optoacoustic microscopy i.e., reaching several millimeters in depth. The approach utilizes tomography to achieve ultrasonic-diffraction resolution and operates at high-ultrasound frequencies (20 to 200 MHz) induced by few-nanosecond laser pulse excitation of tissues. We investigated here the performance of optoacoustic mesoscopy implemented at 24 MHz center frequency and its ability to resolve optical absorption contrast in the mouse kidney *ex vivo*. The developed system achieved better than 30 μm in-plane resolution and 110 μm elevation resolution over a cylindrical volume of 9-mm diameter and 9-mm height. This unprecedented combination of resolution and depth was achieved by implementing a translate-rotate detection geometry and by tomographic reconstruction. The approach yielded images of optically absorbing structures with a level of detail never-before visualized in an intact mouse kidney and allows insights into their unperturbed architecture. We discuss the ability to offer multispectral acquisitions and enable *in vivo* imaging. [DOI: 10.1117/1.JBO.18.10.106005]

Keywords: optoacoustic; mesoscopic scale; linear array; computed tomography; high-frequency ultrasound.

Paper 130441R received Jun. 26, 2013; revised manuscript received Sep. 10, 2013; accepted for publication Sep. 16, 2013; published online Oct. 4, 2013.

1 Introduction

Mesoscopic-scale (i.e., 1-mm to 1-cm-sized) organisms and body parts of small animals remain largely inaccessible by optical imaging due to the high photon-scattering exhibited by most tissues.[1] To enable imaging with optical contrast of diffusive organisms and tissues at mesoscopic scale with a sub-100 μm scale spatial resolution, biomedical optoacoustic (also termed photoacoustic) imaging techniques have been considered instead.[2–8] By visualizing optical absorption at multiple wavelengths, it is further possible to detect the spectral signatures of different chromophores, leading to the visualization of anatomical, physiological, and cellular and subcellular tissue features using endogenous or exogenous contrast.[9]

The resolution in optoacoustic mesoscopy obeys the ultrasonic diffraction limit. In this regime, optoacoustic imaging bears a significant advantage; i.e., it can offer virtually a continuum for resolution and depth by appropriately selecting the frequency band of the transducer capturing the ultrasonic waves generated in tissues in response to excitation with nanosecond laser pulses. Typically the penetration depth for ultrasonic frequencies <40 MHz is dictated by light attenuation, whereas for frequencies >40 MHz, acoustic attenuation becomes stronger than optical attenuation in the near-infrared.[10] Additional parameters that play a role in the resolution and the overall image quality achieved depend on the detection aperture and the spatial sampling frequency by which ultrasonic waves are sampled, and the overall geometry and focusing characteristic of the detector elements.

Current optoacoustic imaging systems that employ high-frequency detectors for three-dimensional (3-D) mesoscopic imaging have used planar detection geometry[11] and acquire tomographic datasets by raster scanning a single point-like detector,[3,12] or spherically focused transducers used in synthetic aperture focusing and performing in and out-of-focus tomographic interrogations.[2,5,13] Linear array implementations in planar mode have also been considered.[4,14] The planar geometry is convenient if only one side of the specimen can be accessed, but, because of the restriction to a finite region of the infinite plane and the directionality of detectors, suffers in practice from a limited angular detection aperture. In consequence, the imaging resolution in the two dimensions parallel to the detection plane is limited by the finite aperture. The limited view also results in the invisibility of directional objects emitting parallel to the detection plane, such as vessels and other absorbing structures stretched in the direction perpendicular to the detection plane.

Recently, a translate and rotate geometry using linear arrays was examined in our group[15] and was shown to extend the angular aperture coverage in comparison to planar geometries while keeping a large field of view. First validated experimentally with a 6 MHz ultrasound array, the geometry was demonstrated to provide a high 3-D resolution (130 μm in-plane and 330 μm in elevation) limited by the detection aperture of the array in only one dimension instead of two, as typical for planar scanners. In this paper, we present a mesoscopic implementation of the translate-rotate geometry using a 24 MHz linear ultrasound array. We hypothesized that this approach will yield superior performance characteristics to planar scanning systems both in terms of resolution and spatial fidelity. The ability to implement such a system was due to the combination of a high-frequency

Address all correspondence to: Vasilis Ntziachristos, Technische Universität München and Helmholtz Zentrum München, Institute for Biological and Medical Imaging, Ingoldstädter Landstraße 1, 85764 Neuherberg, Germany. Tel: +49 (0)89 3187 3852; Fax: +49 (0)89 3187 3008; E-mail: v.ntziachristos@tum.de

0091-3286/2013/$25.00

detector array with a newly developed analog-to-digital converter operating at 125 MHz sampling frequency and precision motor-stages. The system was first characterized with phantoms and its performance then demonstrated on a fresh (not fixed) excised mouse kidney. Moreover, we investigated herein a time-efficient continuous data acquisition method and demonstrate, for the imaged kidney, fast data collection leading to high image quality without averaging.

2 Materials and Methods

2.1 *Experimental Setup*

The experimental setup used in this study is presented in Fig. 1. The implementation of the multidetector translate-rotate scanner is similar to the one described in detail in Ref. 15. To accommodate, however, the high-frequency detectors, a novel data acquisition system was developed and higher-precision motorized scanning stages were selected as described in the following.

Ultrasound detection was performed with a high-frequency 128-element linear array (LA-28.0, Vermon, Tour, France). The elements of the array had an average center frequency of 24 MHz and an average −6 dB two-way (pulse-echo) bandwidth of 60%. The width of one element was 55 μm, with a kerf of 15 μm (i.e., a pitch of 70 μm), and its height (transverse dimension) was 1.5 mm. The elements were cylindrically focused using an acoustic lens. The focal length was ~7.5 mm.

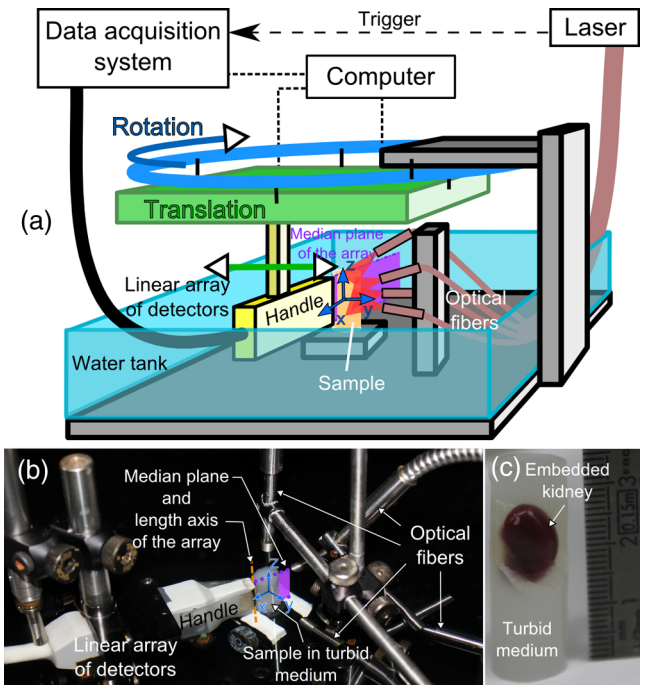

Fig. 1 Experimental setup. (a) Schematic drawing of the optoacoustic translate-rotate scanner showing the arrangement of the motorized stages. The linear array of detectors is mounted on the translation stage. A Cartesian coordinate system, fixed to the sample, is specified. The origin of the system is set so that the z axis corresponds to the rotation axis of the rotation stage and the plane $z = 0$ to the middle of the length of the linear array. The z axis defines the elevation direction of the system. (b) Annotated picture of the experimental setup. (c) Picture of an excised mouse kidney embedded in a turbid agar gel. The upper-front part of the agar gel was removed to disclose the kidney, and a metric steel ruler was placed on the side for size reference.

The geometrical characteristics of the cylindrically focused elements result in a sensitivity field with calculated full width half maximum (FWHM) dimensions in the xy-plane and at 24 MHz of ~300 μm around the focus in the transverse dimension, and longer than 1 cm for the depth-of-field.[16] Detected signals were digitized at 125 MS/s and with a 12-bit resolution over a 16 mV range with a 128-channel custom-built data acquisition system.

The linear array was mounted on two motorized precision stages: a translation stage (M-605.2DD, Physik Instrumente, Karlsruhe, Germany) and a rotation stage (M-062.PD, Physik Instrumente). The stages were equipped respectively with an integrated linear encoder and an integrated rotary encoder, which enabled a reliable assessment of the successive positions of the detector array during tomographic measurements of high-frequency ultrasound field. The encoders provided a micrometric accuracy for both step-by-step motion and readout of the motor positions during continuous motion. The stages were suspended from a platform so that the translation stage was rotated by the rotation stage [Fig. 1(a)]. The linear array was mounted on the translation stage so that its length axis (i.e., the long axis of the active surface of the array, parallel to the focal line of the elements) was parallel to the rotation axis of the rotation stage (z axis in Fig. 1), and its median plane was perpendicular to the translation axis of the stage [Figs. 1 and 2(a)]. The minimal distance between the length axis of the array and the rotation axis was set to $R = 7.5$ mm, i.e., the focal length of the array [Fig. 2(a)]. The data acquisition system and the motors were computer-controlled.

The excitation light originated from a tunable (690 to 900 nm) optical parametric oscillator laser (Phocus II, Opotek Inc., Carlsbad, California), delivering <10 ns duration pulses with a pulse repetition frequency (PRF) of 10 Hz. The beam was guided into a silica fused-end fiber bundle (CeramOptec GmbH, Bonn, Germany) consisting of 640 fibers partitioned into four legs. To spread out light and illuminate the surface of the imaged samples more evenly, all samples were embedded in turbid gel. Turbid gel mimicking the speed of sound in soft tissues was prepared by mixing 1.6% w/m agar gel (Agar for microbiology, Fluka analytical) with 0.8% v/v intralipid-20% (Sigma). The gel was poured around the sample in a cylindrical mold of 12 mm inner diameter and 3.5 cm height so as to form an optically diffusing layer—at least 2 mm thick on the side and 5 mm thick on the top [Fig. 1(c)]. The unmolded cylinder was then inserted in a fixed sample holder so that its axis corresponded to the rotation axis of the stage and the embedded sample faced the ultrasound array. Three legs of the fiber bundle were positioned 2 cm away from the cylinder to create an illumination pattern of ~10 mm height and ~12 mm width on one side (cylinder surface with $y > 0$), and the fourth leg was used to illuminate the top of the cylinder. The illumination was kept fixed for all the samples, and the optical excitation was performed for all the experiments at a single wavelength of 760 nm and with a per-pulse energy at the laser output of ~70 mJ. This wavelength ensures a good penetration in biological tissue.[9] The laser was run continuously at 10 Hz and triggered the acquisition system.

The fiber bundle ends, the ultrasound linear array, and the sample were immersed in a water tank for acoustic coupling. The tank was filled with isotonic saline solution (0.90% w/v of NaCl in deionized water) to preserve the *ex vivo* sample. The solution was stabilized at room temperature.

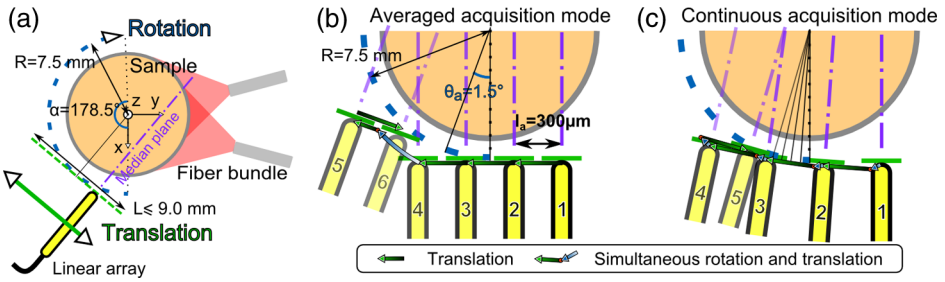

Fig. 2 Scanning procedures. (a) Schematic top view of the experimental setup. Schematic description of the scanning procedures in (b) the averaged acquisition mode, shown here for the first six positions of the array assuming a travel range of four to five positions [complementary patterns (15)] and (c) the continuous acquisition mode, shown here for the first five positions of the array. The positions of the array are indexed with increasing numbers. The diagrams (b) and (c), in particular the motion steps, are not to scale, but were exaggerated to illustrate better the motion of the array.

2.2 *Scanning Procedures*

The optoacoustic imaging system implemented in this study performs a translate-rotate scanning motion of the detector array around the fixed sample to acquire tomographic datasets. Full datasets are obtained by translating the detector array across the sample repetitively and rotating the combined translation stage and detector array until they have been rotated by ~180 deg [Fig. 2(a)]. The translation range can be adapted to the imaged volume and should match or exceed the radial extent of the volume.[15] A rotation range of $\alpha = 178.5$ deg and a maximum translation range L of 9.0 mm were used.

Two different scanning procedures were employed in this study. In the first one, the array was scanned in discrete steps. For each detector position, five time-resolved acquisitions were averaged and the result stored in the computer before advancing to the next position. Averaging was employed to increase the signal-to-noise ratio by reducing electronic noise. The motion sequence alternated between multiple-step translation motions across the sample and single-step increments of the rotation motion [Fig. 2(b)]. This systematic scanning procedure for optoacoustic imaging was described in detail in our previous study[15] and is referred to in this study as averaged acquisition mode. The rotary stage was moved here to a total of 120 positions, with a 1.5 deg angular step (θ_a). Between each rotation step, the array was scanned linearly by moving the translation stage in steps of $l_a = 300$ μm. The array trajectory was then tangent to the circle of radius R centered on the axis of rotation and the positions were distributed symmetrically with respect to the point of tangency [Fig. 2(b)]. For the translation, the sampling requirement is determined by the FWHM of the sensitivity field at the center frequency of the array. The Nyquist sampling criterion implies that the translation step should be at most half of the FWHM of the sensitivity field. The step length l_a corresponds to the FWHM of the sensitivity field at 24 MHz calculated for the fixed cylindrical focus of the array.[16] However, as in our previous study, for two successive translations across the sample, the detector positions along the translation axis were shifted by half the step length to obtain complementary patterns. This scanning feature was implemented to obtain datasets with richer information. For the rotation motion, the angular step from our previous study[15] was also used here as it showed good performance. Assessing the angular sampling requirement in terms of the Nyquist sampling criterion is actually more difficult than for the translation motion because the directivity of both the detector and the structure inside the sample have to be considered (full view criterion). No *a priori* assumption was made on the directivity of the absorbing structures. The angular aperture of the array in the transverse direction was ~11 deg. If we consider translations across the sample by pairs, the angular step was actually 3 deg, which is a reasonable oversampling in regards to the angular aperture of the array.

In the second scanning procedure, the array was continuously and simultaneously rotated and translated [Fig. 2(c)]. For each laser pulse, signals were acquired with the linear array of detectors and stored in the computer without averaging. Readouts of the motor positions given by the motion controllers were stored as well. The rotation stage was moved at constant speed in only one direction to cover the rotation range in the total duration of the scan. The translation stage operated in oscillatory motion, moving back and forth with a predefined speed v_c over the same linear segment. The linear segment was chosen symmetric with respect to the point of tangency between the translation axis and the circle of radius R centered on the axis of rotation [Fig. 2(a)]. For a given translation range L and PRF of the laser, the translation speed v_c and the number of single-pulse acquisitions per period of oscillatory motion were set so that the travel distance of the translation stage between two successive laser pulses $l_c = v_c/\text{PRF}$ was approximately a predefined common fraction of l_a, the step length in the averaged acquisition mode (i.e., 300 μm). The total number of single-pulse acquisitions was then set so as to have 60 periods of oscillatory motion of the translation stage during the scan, and the rotation speed was determined. The number of periods of oscillatory motion was chosen equal to the averaged mode for better comparison. This scanning procedure is named continuous acquisition mode (CAM) in this study. To be able to refer easily to continuous acquisitions of different parameters, a number was associated with each CAM implementation. This number corresponds to the ratio of l_a to l_c, the targeted travel distance of the translation stage between two successive single-pulse acquisitions in the continuous mode. The CAM number was set ≥ 1 to ensure a good spatial sampling. Predetermined and measured parameters of continuous acquisition modes implemented for a translation range of $L = 9.0$ mm are given in Table 1. The observed median travel of the translation stage between successive acquisitions was lower than expected most probably because of the acceleration and deceleration phase while changing direction. Considering the maximum speed of the array during the acquisitions, the Doppler effect induced by the motion of the detectors could be considered as negligible for the measured ultrasound frequencies.[17] The maximum propagation distance for the ultrasound waves being 15 mm, the displacement of the focal spot of the array during the optoacoustic wave propagation could also be considered as negligible.

Table 1 Data acquisition parameters for different modes and a translation range of 9.0 mm.

Data acquisition mode	Averaged	Continuous #					
		1	2	2.5	3	4	5
Total number of measurement positions	3660	3660	7380	9180	10,980	14,700	18,300
Rotation range				178.5 deg			
Mean travel of the rotation stage between successive measurement positions	1.5 deg	2.9′	87.3″	70.2″	58.6″	43.6″	35.1″
Translation range (mm)				9.0			
Median travel of the translation stage between successive measurement positions (μm)	300	296	147	118.5	99	74	59.5
Maximum speed of the array during the acquisitions (mm.s^{-1})	—	3.0	1.5	1.2	1.0	0.8	0.6
Total acquisition time (min)	43.3	6.1	12.3	15.3	18.3	24.5	30.5

CAM #5 and the averaged acquisition mode required collecting the same number of nonaveraged signals. However, in continuous acquisition mode, the single-pulse acquisitions corresponded to successive laser pulses, while in averaged mode, each averaged acquisition started only when the motor was in position. The laser pulses occurring during the detector motion were therefore not used in averaged acquisition mode, which resulted in longer scan times (Table 1).

2.3 *Image Reconstruction and Postprocessing*

Datasets acquired with the scanner were reconstructed on a grid composed of cuboid voxels of 12 μm × 12 μm × 24 μm, with a filtered backprojection algorithm described in detail in Ref. 15. The elevation aperture along the length axis of the array was kept constant and equal to 0.8 as long as possible. Signals were bandpass filtered (Butterworth order 3, cutoff frequencies 2 and 40 MHz).

As the translation range was shown, with the translate-rotate geometry, to define the diameter of a cylinder where image quality in terms of resolution is optimal,[15] the cuboid 3-D images were cropped to remove the outer parts of the cylinder before visualization. The 3-D images were visualized using maximum amplitude projections (MAP) and a rotation around one axis. This visualization was performed with the 3-D project option of ImageJ.

2.4 *Sample Preparation*

As mentioned in Sec. 2.1, all samples were embedded in turbid agar gel and molded to form cylinders of 12-mm diameter.

2.4.1 *Phantoms for characterization and calibration*

Two kinds of calibrated absorbers were inserted in agar gel for the characterization of the optoacoustic system: 20-μm diameter black-colored nylon suture threads (NYL02DS, 10/0, Vetsuture, Paris, France) and 10-μm diameter black polystyrene microspheres (carboxylated polystyrene microparticles, Polysciences Inc., Warrington, PA). With the laser pulse duration used here, these absorbers are expected to generate optoacoustic signals greater than the highest recorded frequency[18,19] and are therefore suited for resolution assessment.

Three phantoms were prepared. The first and second phantoms contained black suture threads arranged respectively in a cross along the length of the cylinder (Phantom 1) and in a two-loop knot (Phantom 2). These phantoms were used to assess the performance of the system in terms of spatial fidelity and separation between two objects. The third phantom was prepared with 10-μm microspheres randomly spread over the entire volume of the phantom (Phantom 3). Phantom 3 was used to assess the performance of the system in terms of 3-D resolution.

2.4.2 *Ex vivo kidney preparation*

A CD1® adult mouse (Charles River Laboratories, Research Models and Services, Germany GmbH) was euthanized, and one of its kidneys was excised for imaging. The kidney was embedded in turbid agar gel and placed in the imaging system <20 min after the animal's death. Mouse husbandry, handling, and euthanasia were performed according to the institutional and Bavarian government regulations in frame of approved animal protocol. A mouse kidney was chosen in this study as a biological sample because of the volumetric and fractal morphology of its vasculature.

After tomographic measurements, the embedded kidney was frozen and sliced with a biological microtome cryostat (Leica CM1950, Leica Biosystems Nussloch GmbH, Nussloch, Germany). Red filtered images (630 ± 30 nm) of the sectioned organ were taken. The colored filter enhances the contrast between blood vessels and surrounding tissues.

3 Results

3.1 *Volumetric Imaging in Averaged Acquisition Mode*

3.1.1 *Spatial fidelity and separation between two objects*

Figure 3 displays the reconstructions of Phantom 1 and Phantom 2, composed of 20-μm diameter suture threads arranged in a cross and a loose two-loop knot, respectively. The continuous and controlled structures were scanned in averaged acquisition mode with translation ranges of 5.1 mm. The complex shape of the absorbers could be reconstructed in a volume about the height of the array [Figs. 3(a) and 3(d)] with a consistent resolution over the

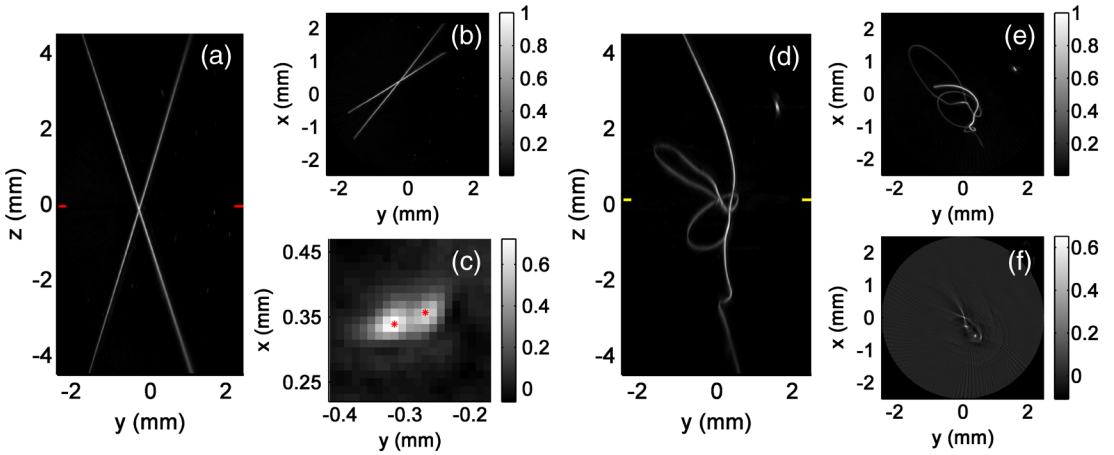

Fig. 3 Reconstructions of Phantom 1 [(a) to (c)] and Phantom 2 [(d) to (f)], both composed of Ø 20 μm threads arranged respectively in a cross and a loose two-loop knot (Video 1). (a) and (b) Maximum amplitude projection (MAP) images respectively along the x axis and the z axis of the first phantom. (c) Two-dimensional slice corresponding to the plane marked with superimposed marks on the sides of (a). The star markers indicate the position of the maxima corresponding to the reconstruction of each thread. The distance between the two stars is 51 μm. (d) and (e) MAP images respectively along the x axis and the z axis of the second phantom. (f) Slice corresponding to the plane marked with superimposed marks on the sides of (d). The images are normalized by the maximum value of the three-dimensional (3-D) images. (Video 1, QuickTime, 2.1 MB) [URL: http://dx.doi.org/10.1117/1.JBO.18.10.106005.1].

volume [Figs. 3(a) and 3(b)] and the multiple orientations [Figs. 3(d) and 3(e)]. One can also notice that dust particles trapped in the solid gel were reconstructed, including a large and strongly absorbing one in the second phantom around $z \sim 3$ mm [Figs. 3(d) and 3(e)]. A slice orthogonal to the z axis was selected from the reconstruction of Phantom 1 [Fig. 3(c)] close to the location of the intersection of the threads. This slice corresponds to the slice where the saddle point between the individual reconstructions of the threads first develops. The distance between the two maxima corresponds to the resolution in the sense of the Sparrow resolution criterion. It was determined here to be 51 μm. A second slice was taken from the reconstruction of Phantom 2 at the location of an in-plane (orthogonal to the z axis) intersection of the thread [Fig. 3(f)]. This slice shows cross-sections of portions of the thread with different orientations, reconstructed with the measured tomographic dataset. Figure 3(f) reveals that objects with an elongated in-plane cross-sectional area lead to strong arc-shaped streaking artifacts in the background. For instance, artifacts in the part of the image with $x < -1$ mm and $y > -1$ mm are due to the crossing portions of the thread. These arc-shaped artifacts are produced by the simple radial backprojection algorithm used here for reconstruction[20] and the finite number of angular steps of the scan geometry. The backprojection artifacts appear weaker for objects with an isotropic in-plane cross-sectional area like the portions of the thread mainly oriented toward the z axis, which can be explained by the fact that the translate-rotate scanning geometry averages spatially the artifacts produced by such objects over more projections distributed on a larger solid angle of detection. The streak artifacts are not visible on the MAP images as they have lower amplitude than the main lobes. Negative and nonphysical values also appear on the slices [Figs. 3(c) and 3(f)], and are also filtered backprojection artifacts.

3.1.2 *Resolution of isotropic objects*

The third phantom, composed of Ø 10-μm microspheres randomly spread in the turbid agar gel, was imaged with the system using a translation range of 9.0 mm. Figures 4(a) and 4(b) show MAP images of the reconstruction of a 2.1-mm-thick (along the z axis) slice of Phantom 3. The slice thickness was chosen such that microspheres are spread all over the diameter of the imaged volume but remain distinct and well separated in the MAP images. Microspheres at different in-plane [Fig. 4(a)] and elevation [Fig. 4(b)] positions were reconstructed. Besides amplitude variations due to light scattering, and a thresholding of the brighter voxels, all microspheres were reconstructed with a vertical rice-grain shape and 3-D resolutions consistent over the volume of the slice.

The 3-D resolution of three microspheres located at different polar (along the x and y axes) and elevation coordinates was analyzed. Cuboid volumes that centered the microspheres ($9 \times 9 \times 11$ voxels) were extracted from the 3-D image [superimposed rectangles, Figs. 4(a) and 4(b)]. The MAP of these cuboids in two orthogonal planes are displayed in Figs. 4(c) to 4(e). The MAP images along the z axis show that microspheres are resolved identically along the x and y directions. The FWHM dimensions of the MAP profiles for the three microspheres were determined to be equal to (mean $\pm$ standard deviation) 29 ± 2 μm in plane (along the y axis) and 110 ± 5 μm in elevation. By taking into account convolution effects between the finite size of the microsphere and the impulse response of the system, this measurement points to an in-plane system resolution of <30 μm. The discrepancy between the two resolutions is due to the angular coverage difference induced by the limited aperture of the array along the z axis.

The in-plane FWHM dimensions of the microspheres are smaller than the in-plane resolution determined with Phantom 1. Although the microspheres have a smaller diameter than the threads, both types of absorbers are expected to emit optoacoustic wave with a peak frequency greater than the highest recorded frequency.[18,19] The difference in in-plane resolution is then most probably due to the coupling between in-plane and elevation resolution for the elongated absorbing threads intersecting the xy plane with an angle.

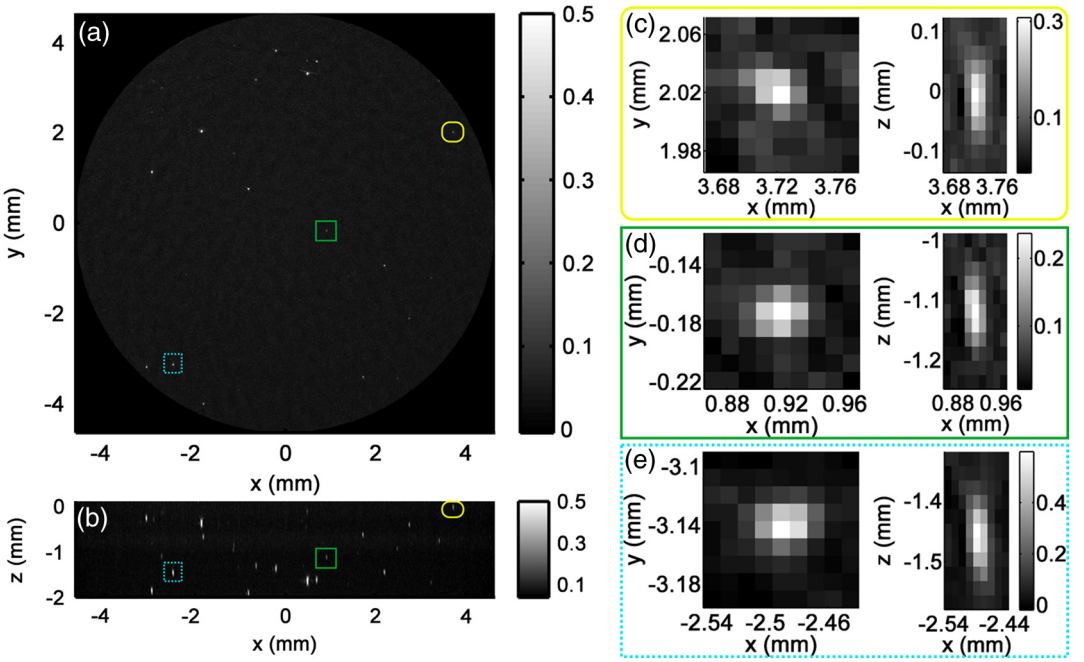

Fig. 4 Reconstruction of a 2.1-mm-thick volumetric slice of Phantom 3 (comprising Ø 10 μm microspheres randomly spread over the volume). (a) MAP image along the z axis. (b) MAP image along the y axis. The superimposed rectangles indicate the limits of three subregions of interest. (c), (d), and (e) MAP images of these subregions along the z axis (left) and the y axis (right). The amplitude of the images is normalized by the maximum value of the 3-D image. (a) and (b) are thresholds for better visualization.

3.1.3 *Ex vivo anatomic images of mouse kidney*

An excised kidney of an adult mouse was imaged *ex vivo* using a translation range of 9.0 mm. The MAP image along the x axis is presented in Fig. 5(a). The bean-shaped structure of the kidney was positioned vertically, with the convex surface toward the illumination side. The superior part of the kidney was imaged. The renal hilum is located around $z \sim -2.4$ mm. Structures of the renal vascular anatomy can be visualized with MAP [Fig. 5(a) and Video 2], in particular by decreasing size and from the renal hilum to the renal cortex, dividing segmental, interlobar, and interlobular vessels. The volumetric vascular morphology visible with the obtained MAP images show similar structure as images obtained from vascular corrosion casts of mouse kidneys.[21] Because of the inhomogeneity of the light fluence with depth, only the portion with the stronger illumination is seen on the MAP images. Correction schemes for fluence have been suggested in the literature[22,23] and will be considered as a next step of the mesoscopic setup development.

Two different slices of the 3-D image, taken around the renal hilum, are displayed in Figs. 5(b) and 5(d) and show that vessels could be imaged over the entire organ, reaching up to 10 mm away from the illuminated surface ($y < 0$). Photographs of the frozen and sectioned organ for these corresponding slices are presented in Figs. 5(c) and 5(e). Black areas on these photographs are either due to blood vessels or the empty renal pelvis. As they correspond to the same kidney, the photographs validate the optoacoustic images, even if mostly large blood vessels can be correlated due to the intrinsic lack of contrast of the photographs. The renal pelvis being nonabsorbing, it could not be directly imaged with the optoacoustic system. The vascular anatomical features were also correlated with published anatomy.[24]

The kidney was used here as a biological sample for the multiple size and branching vasculature of this organ. Despite the limited bandwidth of the array that induces a sensitivity dependence on the object size, the reconstruction demonstrated that the developed optoacoustic system was able to resolve at least five orders of vessel branching, from the renal vein to interlobular vessels. Many microvessels—arcuate as well as interlobular arteries and veins—could be resolved in the renal cortex [Video 2, Figs. 5(b) and 5(d)]. The filament-like structure of the vasa recta in the medullary region could even be visualized [Fig. 5(d)] while composed of capillaries.[21]

3.2 *Continuous versus Averaged Acquisition Mode*

The mouse kidney imaged in averaged acquisition mode (Fig. 5) was scanned successively in the CAMs, listed in Table 1. Reconstructions of the two slices (slices #1 and # 2) shown in Fig. 5 for the averaged acquisition mode are presented in Fig. 6 for CAM #1, #2.5, and #5. The number of measurement positions in the averaged acquisition mode and in CAM #1 was equal (Table 1). The number of single-pulse acquisitions in the averaged acquisition mode and in CAM #5 was equal. CAM #2.5 had an intermediate number of single-pulse acquisitions.

The image quality for the visualization of the renal artery and renal vein in slice #1, and the medullary region with the vasa recta in slice #2 increased significantly between the averaged acquisition mode and CAM #5 while the same number of single-pulse acquisitions was used. As for the knot (Fig. 3), strong arc-shaped streaking artifacts are visible for the kidney in the reconstructions of slices #1 and #2 corresponding to the averaged acquisition mode (full arrows Fig. 6). These artifacts impair the image contrast and block the visualization of fine details by increasing locally the background noise. This type of streak artifacts mostly arises from structures elongated in-plane. Figure 6 shows a streak artifact reduction with the increased CAM number, while the same filtered backprojection algorithm was used. The artifacts in CAM #1 were similar but

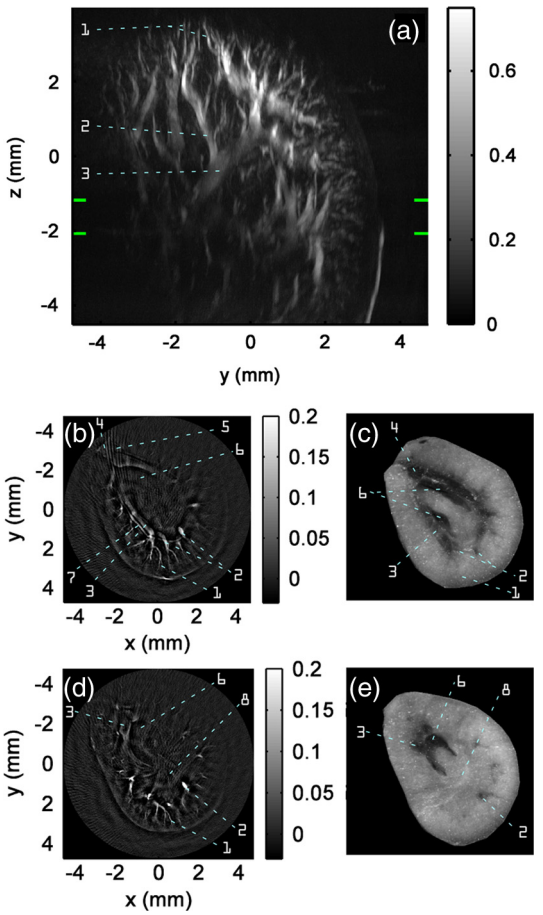

Fig. 5 Reconstructions of the kidney of an adult mouse. (a) MAP images along the *x* axis. The superimposed marks on the sides of (a) indicate the positions of two in-plane slices. The slices are presented ordered by increasing *z*: (b) slice#1 and (d) slice#2. The images are normalized with the maximum voxel value of the 3-D image and threshold for better visualization. (c) and (e) Red-filtered photographs of the frozen and sectioned kidney corresponding respectively to slice #1 and slice #2. Legend: 1, interlobular vessels; 2, interlobar vessels; 3, segmental veins; 4, renal vein; 5, renal artery; 6, renal pelvis; 7, segmental artery; 8, medullary region with the vasa recta. The anatomical features were correlated with published anatomy.[24] (Video 2, QuickTime, 3.5 MB) [URL: http://dx.doi.org/10.1117/1.JBO.18.10.106005.2].

already lower than in average acquisition mode. Therefore, this type of streak artifacts occurs here if too few views of the sample were obtained. Continuous acquisitions increased the number of views of the sample since the array was constantly moving while keeping the number of single-pulse acquisitions inferior or equal to the average mode.

In areas free of strong artifacts, some interlobular vessels clearly visible in averaged acquisition mode (empty arrows Fig. 6) could not be visualized in CAM #1 and hardly in CAM #2.5. Two factors could be responsible. First, as reconstructions for CAM #1 and #2.5 use datasets collected with less single-pulse acquisitions than in averaged acquisition mode, electronic noise reduction by averaging is weaker and therefore the background noise of the image could be stronger. Second, as in continuous acquisition mode, the angular position of the rotation stage is different for each measurement; the number of views for a directional absorbing structure could be lower than with a systematic scanning across the sample for each angular step. To test the first hypothesis, the standard deviation of background noise was computed in the same cuboid volume of $21 \times 21 \times 21$ (i.e., 9261) voxels (around slice #2 and marked with a superimposed square in Fig. 6) for all the acquisition modes (Table 1). The results are displayed in Fig. 7 and show that the background noise decreases with the CAM number. In comparison to the averaged acquisition mode, the background noise was found 65% stronger in CAM #1, 31% weaker in CAM #5, and only 5% stronger in CAM #2.5. These results indicate that the noise level could be a dominant factor to explain the nonappearance of some interlobular vessels in CAM #1. The background noise was found very similar for the averaged acquisition mode and CAM #2.5 while half the number of single-pulse acquisition was used for the latter, and lower for CAM number superior or equal to 3. The background noise is therefore mostly due to the streak artifacts in averaged mode, and to electronic noise for CAMs with numbers <2.5. For CAM #2.5, the limited number of views could explain the contrast difference for the spotted interlobular vessels.

Phantom 3, composed of Ø 10-μm black microspheres (Fig. 4), was also imaged in continuous modes with numbers ranging from 1 to 5. Besides an increase of the background noise for CAM with numbers <3, the 3-D resolution of the

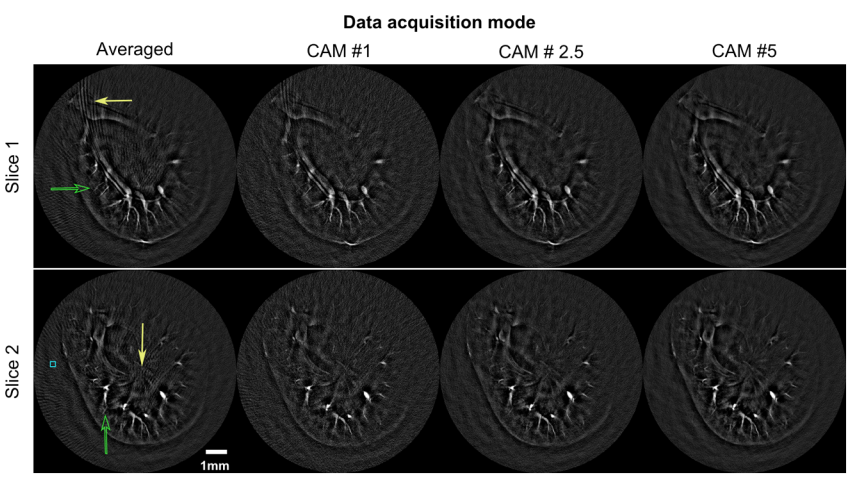

Fig. 6 Reconstructions of slices #1 (top row) and #2 (bottom row) of the mouse kidney for several acquisition modes. The full arrows indicate regions where image quality is affected by arc-shaped streaking artifacts in average acquisition mode. The empty arrow points at interlobular vessels; the visibility of these vessels depends on the acquisition mode. The superimposed square indicates the limits of the regions for which the standard deviation of the background noise was assessed.

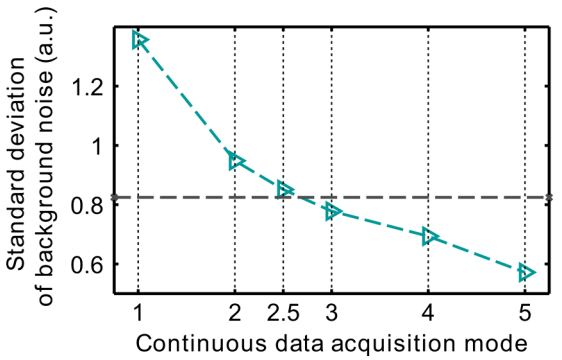

Fig. 7 Standard deviation of the background noise as a function of the number of continuous data acquisition modes for the volumetric image of the kidney. The standard deviation was computed in $21 \times 21 \times 21$ voxel cuboids. Each volumetric image was normalized by the number of measurement positions. The horizontal dashed line corresponds to the value in averaged data acquisition mode.

three microspheres analyzed in Sec. 3.1.2 (Fig. 4) was found unchanged between averaged or continuous modes.

In brief, continuous acquisition modes have the advantages of reducing the scan time, the backprojection streaking artifacts, and the background noise, without any drawbacks except for the large size of the tomographic datasets generated, and therefore the computationally demanding reconstructions.

4 Discussion

We examined in this study the performance of a translate-rotate scanner employing a high-frequency linear array and a full-field illumination for volumetric optoacoustic tomography at mesoscopic scale. The study demonstrated that the proposed implementation provides a system able to image specimen as large as 9 mm in size, with a high spatial fidelity and a sub-30 μm resolution in two dimensions and on the order of 100 μm in the third one. To make optimal use of the experimental configuration, we investigated the role of the scanning procedure, averaged or continuous, on the achieved image quality and scanning time. Continuous acquisition enables an increase in the number of angular orientations available to tomographic views and reduces the scanning time over averaged acquisition. With continuous acquisition, the scanning time could be reduced by more than a factor of two for similar image quality of *ex vivo* biological tissue.

The use of an existing and commercially available linear array of detectors was a convenient means of implementing a high-frequency and volumetric optoacoustic imaging system that exploits the capabilities of parallel channel data acquisition over a 9 mm detection aperture, and the recent advances in piezoelectric array technology.[25–28] To our knowledge, for technical reasons, currently only linear and annular[29] piezoelectric arrays have been developed for frequencies >20 MHz. Our linear array had a pitch of 70 μm for a center frequency of 24 MHz and, therefore, presents an adequate spatial sampling along its length axis. The receiving elements were cylindrically focused to increase their surface area and therefore enhance their sensitivity. Moreover, the relative aperture in the transverse direction was set to an f-number of 5 to obtain a large depth of field in the axial direction.[16] The translate-rotate geometry implemented here scanned the focal spot within the sample so that the full-view criterion was fulfilled in-plane. As it maintains the focal spot inside the sample and the array close to the sample, the scanning geometry was demonstrated to be especially adapted to acquire the high-frequency components of the optoacoustic field for which the emission efficiency is weaker[30] and the attenuation is stronger[10] than mid-range medical ultrasound frequency (3 to 10 MHz) components.

The developed system shows an unprecedented combination of imaged volume, angular detection aperture, and high 3-D resolution for optoacoustic mesoscopy. Fulfilling the full view criterion in plane and taking advantage of the limited but large aperture of the array in the elevation direction (z axis), the system achieved a high spatial fidelity as shown with Phantom 2 comprising a knot thread with multiple orientations [Figs. 3(d) to 3(f)], and limited the number of invisible objects. Only directional objects emitting mostly in the z direction such as an absorbing layer thin in the elevation direction and extended in-plane will hardly be visible. The in-plane FWHM dimensions for 10-μm diameter microspheres were found to be ~29 μm for the detection geometry and reconstruction algorithm selected in this study. The acoustic wavelength in the medium corresponding to the low-pass cutoff frequency of the system (40 MHz) is $\lambda_c \approx 37$ μm, which implies that the reconstructed in-plane FWHM dimensions of the sphere match the optimal resolution achievable theoretically [$0.8\ \lambda_c \approx 30$ μm (Ref. 31)]. The in-plane resolution was found consistent over the radial dimension of the imaged volume (Fig. 4). Because of the limited view in the elevation direction, the elevation resolution was lower for the isotropic absorbers, and the ratio of the elevation to the in-plane FWHM dimensions of the microspheres was ~3.8. This ratio was 2.6 in our previous study with the 6 MHz array.[15] The significant difference can be attributed to the higher ratio between the focal distance and the aperture length of the array in the present study. The dynamic aperture adjustment in elevation was only done with an f-number of 0.8 here, instead of 0.5 in Ref. 15.

A simple radial backprojection algorithm was used here for image reconstruction because of its easy implementation. However, as shown in Figs. 3 and 6, despite the great number of measurements made with the detectors in average acquisition mode, reconstructed images have arc-shape streaking artifacts. These artifacts are mainly visible for absorber with in-plane directionality and, therefore, result from an angular undersampling for the employed reconstruction method. The problem was solved by increasing the number of views and in particular the number of positions of the rotation stage at which data were acquired with continuous acquisition modes (Fig. 6). To obtain a similar level of background noise, we found that the number of measurement positions had to be increased by at least a factor 2.5 (Fig. 7). Even if the acquisition time was lower, the reconstruction time and computational expense increased. As backprojection is nonoptimal in terms of image quality, iterative reconstruction methods have been developed to reduce the associated artifacts.[20,32,33] These model-based methods showed to give better image quality with a lower number of measurement positions.[32,34] They can also take into account the spatial impulse response of the detectors[2,35] and correct the effects of inhomogeneous surface illumination of scattering samples.[22,23] Consequently, the use of an iterative reconstruction method to reconstruct the tomographic datasets acquired with the developed system is expected to further decrease the scanning time and significantly improve image quality. However, such methods cannot currently handle the combined large number of voxels required for high-resolution mesoscopic imaging

[on the order of 10^8 for Fig. 5(a)] and the size of the dataset generated with the translate-rotate scanner for sufficient radial and angular sampling. Furthermore, the methods rely on inversion techniques and are in consequence sensitive to noise. The investigations of the practical implementation of a model-based reconstruction method for our high-frequency system are beyond the scope of this paper, but are of great interest and will be considered in future studies.

Precision stages, continuous acquisition, and simultaneous parallel 128-channel data acquisition optimized the measurement time of tomographic datasets. In comparison with our previous study,[15] the acquisition speed is now primarily limited by the laser pulse repetition frequency. The use of a different laser technology, enabling high-power nanosecond pulse laser with PRF >50 Hz in the near-infrared, would significantly improve the scanning time. Such lasers are commercially available and have been used for mesoscopic imaging by other groups.[12] For the continuous acquisition mode, the maximum speed of the array would have to be maintained low to avoid Doppler effect and large displacement of the focal spot during the measurement, but in particular for CAM #5, where the translation and rotation speeds are currently low, the use of a higher PRF will open the possibilities to perform a tomographic acquisition in a few minutes.

The 3-D image of the vascular morphology of the fresh (not fixed) kidney (Fig. 5 and Video 2) matches the images obtained with an x-ray microCT scanner after injecting contrast agent,[36] or with corrosion casts prepared by replacing blood volume with resin.[37] All these vascular imaging modalities operate *ex vivo*, have the advantage of preserving the 3-D anatomical structure, and do not require any sectioning that could mechanically damage the sample. However, for microCT tomography and vascular casting, the contrast is given by the injection of toxic materials in the blood vessels before sacrificing the animal, while for optoacoustic imaging, the contrast is endogenous. The vascular imaging can therefore be done *in vivo* with optoacoustic imaging[12,38] and additional structures[39] or physiological processes revealed by exogenous contrast[40] can be imaged at the same time. The optoacoustic scanner presented in this study could be used for *in vivo* imaging by selecting a body part that can be constrained in a semi-circular U-shape of 12-mm diameter. Subcutaneous tumors and limbs of murine models or small animals[7] would be suited for imaging by using an appropriate animal holder, preventing motion. The development of such a holder is beyond the scope of this paper and will be investigated in the near future.

For specimens with linear dimensions much larger or much smaller than 12 mm, the translate-rotate scanning geometry of the same high-frequency linear array could be adapted to acquire tomographic datasets with the largest possible angular detection aperture. To release the constrain of enclosing the sample, the scanning geometry recently proposed by Preisset et al.,[41] where the detection geometry is planar and rotation axis of the linear array corresponds to its length axis, could be adapted to the high-frequency array. However, the range of accessible inclination angle would be geometrically limited, and for large inclination angles, the focal spot would be partially out of sample and the sensitivity to high-frequency components of the ultrasound field therefore lower. The full view criteria would consequently no longer be fulfilled in plane. Conversely, for small samples, the enclosure could be larger by tilting the array in the elevation direction and therefore increasing the detection aperture in this dimension.

Finally, with the continuous acquisition mode, the current implementation of the high-frequency system enables multiple successive tomographic acquisitions of the same sample within a time frame on the order of 1 h. Therefore, slow varying biological processes such as the accumulation and potential clearance of exogenous absorbers in lymph vessels and nodes[14] or in tumorous tissues[40] could be imaged *in vivo* at different time points and at 3-D high resolution within a 1-cm-size body part. Successive acquisitions at different excitation wavelengths would allow multispectral optoacoustic tomography[9] and therefore molecular imaging *in vivo* or *ex vivo*, in the volume of an organ as large as a mouse kidney and with a sub-100 μm resolution. The system as a tool for studying pathophysiological processes will be investigated in the near future and is expected to find applications in biological studies of small animals and tissues.

Acknowledgments

The authors thank Nicolas Bézières and Panagiotis Symvoulidis from the Institute for Biological and Medical Imaging for fruitful discussions. We also would like to thank Sarah Glasl and Uwe Klemm for their technical support and the laboratory mouse handling. The research leading to these results has received funding from the European Union (European Research Council, ERC-2008-AdG) under grant agreement no. 233161, MSOT and by the Price for "founding offensive biotechnology" (Go-Bio, 2010) of the Federal Ministry of Education and Research (BMBF).

References

1. V. Ntziachristos, "Going deeper than microscopy: the optical imaging frontier in biology," *Nat. Methods* **7**(8), 603–614 (2010).
2. M. Á. A. Caballero et al., "Model-based optoacoustic imaging using focused detector scanning," *Opt. Lett.* **37**(19), 4080–4082 (2012).
3. E. Zhang, J. Laufer, and P. Beard, "Backward-mode multiwavelength photoacoustic scanner using a planar Fabry-Perot polymer film ultrasound sensor for high-resolution three-dimensional imaging of biological tissues," *Appl. Opt.* **47**(4), 561–577 (2008).
4. L. Song et al., "Fast 3-D dark-field reflection-mode photoacoustic microscopy in vivo with a 30-MHz ultrasound linear array," *J. Biomed. Opt.* **13**(5), 054028 (2008).
5. R. Ma et al., "Fast scanning coaxial optoacoustic microscopy," *Biomed. Opt. Express* **3**(7), 1724–1731 (2012).
6. D. Razansky, C. Vinegoni, and V. Ntziachristos, "Imaging of mesoscopic-scale organisms using selective-plane optoacoustic tomography," *Phys. Med. Biol.* **54**(9), 2769 (2009).
7. D. Razansky et al., "Multispectral opto-acoustic tomography of deep-seated fluorescent proteins in vivo," *Nat. Photonics* **3**(7), 412–417 (2009).
8. R. Ma et al., "Non-invasive whole-body imaging of adult zebrafish with optoacoustic tomography," *Phys. Med. Biol.* **57**(22), 7227–7237 (2012).
9. V. Ntziachristos and D. Razansky, "Molecular imaging by means of multispectral optoacoustic tomography (MSOT)," *Chem. Rev.* **110**(5), 2783–2794 (2010).
10. X. L. Dean-Ben, D. Razansky, and V. Ntziachristos, "The effects of acoustic attenuation in optoacoustic signals," *Phys. Med. Biol.* **56**(18), 6129–6148 (2011).
11. P. Beard, "Biomedical photoacoustic imaging," *Interface Focus* **1**(4), 602–631 (2011).
12. J. Laufer et al., "In vivo preclinical photoacoustic imaging of tumor vasculature development and therapy," *J. Biomed. Opt.* **17**(5), 056016 (2012).

13. M. Omar, J. Gateau, and V. Ntziachristos, "Raster-scan optoacoustic mesoscopy in the 25–125 MHz range," *Opt. Lett.* **38**(14), 2472–2474 (2013).
14. L. Song et al., "High-speed dynamic 3D photoacoustic imaging of sentinel lymph node in a murine model using an ultrasound array," *Med. Phys.* **36**(8), 3724–3729 (2009).
15. J. Gateau et al., "Three-dimensional optoacoustic tomography using a conventional ultrasound linear detector array: whole-body tomographic system for small animals," *Med. Phys.* **40**(1), 013302 (2013).
16. T. D. Khokhlova, I. M. Pelivanov, and A. A. Karabutov, "Optoacoustic tomography utilizing focused transducers: the resolution study," *Appl. Phys. Lett.* **92**(2), 024105 (2008).
17. R. Ma et al., "Multispectral optoacoustic tomography (MSOT) scanner for whole-body small animal imaging," *Opt. Express* **17**(24), 21414–21426 (2009).
18. M. I. Khan and G. J. Diebold, "The photoacoustic effect generated by an isotropic solid sphere," *Ultrasonics* **33**(4), 265–269 (1995).
19. M. I. Khan and G. J. Diebold, "The photoacoustic effect generated by laser irradiation of an isotropic solid cylinder," *Ultrasonics* **34**(1), 19–24 (1996).
20. G. Paltauf et al., "Iterative reconstruction algorithm for optoacoustic imaging," *J. Acoust. Soc. Am.* **112**(4), 1536–1544 (2002).
21. R. Wagner et al., "High-resolution imaging of kidney vascular corrosion casts with nano-CT," *Microsc. Microanal.* **17**(02), 215–219 (2011).
22. T. Jetzfellner et al., "Optoacoustic tomography with varying illumination and non-uniform detection patterns," *J. Opt. Soc. Am. A* **27**(11), 2488–2495 (2010).
23. J. Laufer et al., "Quantitative determination of chromophore concentrations from 2D photoacoustic images using a nonlinear model-based inversion scheme," *Appl. Opt.* **49**(8), 1219–1233 (2010).
24. M. Schünke et al., *Thieme Atlas of Anatomy: Neck and Internal Organs*, Thieme Medical Publishers Incorporated, New York (2010).
25. J. A. Brown et al., "Fabrication and performance of a 40-MHz linear array based on a 1–3 composite with geometric elevation focusing," *IEEE Trans. Ultrason. Ferroelectr. Freq. Control* **54**(9), 1888–1894 (2007).
26. J. M. Cannata et al., "Development of a 35-MHz piezo-composite ultrasound array for medical imaging," *IEEE Trans. Ultrason. Ferroelectr. Freq. Control* **53**(1), 224–236 (2006).
27. F. S. Foster et al., "A new 15–50 MHz array-based micro-ultrasound scanner for preclinical imaging," *Ultrasound Med. Biol.* **35**(10), 1700–1708 (2009).
28. S. Michau, P. Mauchamp, and R. Dufait, "Piezocomposite 30 MHz linear array for medical imaging: design challenges and performances evaluation of a 128 elements array," in *Ultrasonics Symp.*, pp. 898–901, IEEE (2004).
29. H. R. Chabok et al., "A high-frequency annular-array transducer using an interdigital bonded 1–3 composite," *IEEE Trans. Ultrason., Ferroelectr. Freq. Control* **58**(1), 206–214 (2011).
30. G. J. Diebold, "Photoacoustic monopole radiation: waves from objects with symmetry in one, two and three dimensions," in *Photoacoustic Imaging and Spectroscopy*, L. V. Wang, Ed., pp. 3–17, Taylor & Francis Group, London (2009).
31. M. Xu and L. V. Wang, "Analytic explanation of spatial resolution related to bandwidth and detector aperture size in thermoacoustic or photoacoustic reconstruction," *Phys. Rev. E* **67**(5), 056605 (2003).
32. J. Provost and F. Lesage, "The application of compressed sensing for photo-acoustic tomography," *IEEE Trans. Med. Imag.* **28**(4), 585–594 (2009).
33. X. L. Dean-Ben et al., "Accurate model-based reconstruction algorithm for three-dimensional optoacoustic tomography," *IEEE Trans. Med. Imag.* **31**(10), 1922–1928 (2012).
34. K. Wang et al., "Investigation of iterative image reconstruction in three-dimensional optoacoustic tomography," *Phys. Med. Biol.* **57**(17), 5399–5423 (2012).
35. A. Rosenthal, V. Ntziachristos, and D. Razansky, "Model-based optoacoustic inversion with arbitrary-shape detectors," *Med. Phys.* **38**(7), 4285–4295 (2011).
36. M. Marxen et al., "MicroCT scanner performance and considerations for vascular specimen imaging," *Med. Phys.* **31**(2), 305–313 (2004).
37. H. J. S. B. Filho et al., "Pig kidney: anatomical relationships between the renal venous arrangement and the kidney collecting system," *J. Urol.* **179**(4), 1627–1630 (2008).
38. F. Kiessling, D. Razansky, and F. Alves, "Anatomical and microstructural imaging of angiogenesis," *Eur. J. Nucl. Med. Mol. Imaging* **37**(S1), 4–19 (2010).
39. L. V. Wang and S. Hu, "Photoacoustic tomography: in vivo imaging from organelles to organs," *Science* **335**(6075), 1458–1462 (2012).
40. M.-L. Li et al., "In-vivo photoacoustic microscopy of nanoshell extravasation from solid tumor vasculature," *J. Biomed. Opt.* **14**(1), 010507 (2009).
41. S. Preisser et al., "Vessel orientation-dependent sensitivity of optoacoustic imaging using a linear array transducer," *J. Biomed. Opt.* **18**(2), 026011 (2013).